Towards more homogeneous character in 3D printed photopolymers by the addition of nanofillers

Mariola Robakowska [a], Ian Gibson [b], Remko Akkerman [c], Frederik R. Wurm [d], Hubert Gojzewski [d,*]

[a] *Institute of Chemical Technology and Engineering, Faculty of Chemical Technology, Poznan University of Technology, 60-965, Poznan, Poland*
[b] *Department of Design, Production and Management, Faculty of Engineering Technology, University of Twente, 7522 NB, Enschede, the Netherlands*
[c] *Chair of Production Technology, Faculty of Engineering Technology, University of Twente, 7522 NB, Enschede, the Netherlands*
[d] *Sustainable Polymer Chemistry, Department of Molecules & Materials, MESA+ Institute for Nanotechnology, Faculty of Science and Technology, University of Twente, 7522 NB, Enschede, the Netherlands*

A B S T R A C T

The performance of 3D printed materials differs from that of fully cured polymer materials because of the presence of interfacial areas between consecutively joined layers. These interfaces result in an inhomogeneous character of the printed objects and is frequently reported as their main cause of failures. We noted that the presence of nanosilica particles strengthens the 3D printed layers of the polymer matrix by inducing its additional crosslinking. A model resin composed of poly (ethylene glycol) diacrylate (PEGDA) and nanosilica (Aerosil R972) is used for vat photopolymer 3D printing. Evolution of the interface properties at different nanosilica loadings is tracked by mapping its surface stiffness (Young's modulus mapping) using quantitative Atomic Force Microscopy (AFM). Our research demonstrates that incorporating 6% w/v nanosilica in the polyPEGDA matrix unifies its mechanical properties within the layer, leading to a substantial reduction of microscopic inhomogeneity in the final 3D printed materials.

1. Introduction

Additive manufacturing (AM), also known as three-dimensional (3D) printing, has revolutionized the process of building objects from a 3D CAD model using layer-by-layer processing [1,2]. Nowadays, 3D printing is appreciated as a versatile technology in industry, medicine, aerospace and science for its ability to manufacture complex objects with great geometrical freedom, with cost efficiency and material sustainability at the forefront, ready to be robot- or Artificial Intelligence-assisted [1–9].

All 3D-printed objects are microscopically inhomogeneous on considering the way they are manufactured. Building in 3D printing involves bonding layers in different physical and chemical routes, depending on the material (e.g., metals, ceramics, polymers) and processes involved (e.g., extrusion, jetting, fusion, curing). Independent of the object building attributes (materials, process, printing parameters, etc.) an interface between consecutively printed layers always occurs [10–13]. The interface is a boundary that reveals other properties than those associated with the rest of the printed layers, thus resulting in

inhomogeneous properties of the 3D printed objects. The interface has a critical impact on the overall performance, primarily on material fracture resistance [14,15], interlayer adhesion strength [16–18], stimuli-response effectiveness in, so-called, 4D printed materials [19, 20], control of the macromolecular architecture [21,22], and is frequently reported as the cause of failures in printed objects [23–25]. The latter especially occurs when material is printed in the upright configuration (z-axis) and subjected to loads normal to the build plane [26]. Interfacial phenomena in 3D-printed materials remains poorly studied, with only a few systematic research articles offering limited quantitative microscopic analysis [17,18,27–29]. However, it plays a crucial role in enhancing the performance of 3D printed structures, necessitating further research development in this area.

Among 3D printing techniques Stereolithography (SL) is a substantially developed process to obtain polymer objects [3,4]. In short, SL cures a photosensitive liquid resin placed in a vat by laser ultraviolet (UV) beam, forming a thermoset by photopolymerization [30]. The literature reports that acrylate-based resins are the most frequently used for vat photopolymer 3D printing [31]. As an alternative to lasers, SL can

also use selectively masked UV light sources, speeding up the process by curing layers in one step with array devices like Digital Mirror Devices (DMDs) or Liquid Crystal Displays (LCDs) [4,32]. SL has gained a tremendous interest due to high printing accuracy and an increasing number of synthetic and natural polymers that can be processed [7], including those for tissue engineering [33,34] and for functional applications (e.g., shape-memory, microfluidic, highly-stretchable, conductive) [35–39]. It should be noted, however, that many of these materials are mostly pure polymers with intrinsically limited mechanical properties. Subsequently, polymer composites were proposed for 3D printing to attain higher-performance materials with greater structural and functional properties, including tuneability [40–44]. Adding fillers to the polymer matrix leads to synergistic properties of the final material that has implications for the 3D printing process itself. For example nanoparticle dispersion and stabilization needs to be controlled also throughout the build process [20,32,40,45]. While these aspects have been relatively well studied, the question remains: how do filler particles affect the behaviour of the interface and material across the layers in terms of their orientation, aggregation, and interaction with the matrix and curing UV light, considering that the interface can contain individual regions [11,29,46]? The study of the relationships between macromolecules and fillers regarding structure and properties at the interface and its vicinity can offer valuable insights, potentially being instrumental in achieving strong interlayer bonds and greater bulk homogeneity in 3D printed materials. Unfortunately, quantitative characterizations for use across joining regions are limited [11,24,28,29,47], and usually refer to methods that treat the interface as homogenous, which is a substantial simplification [10,13,17,18,48]. In fact, the interfaces of nanocomposites produced through vat photopolymer 3D-printing are not well studied.

In this work, we consider a model polymer nanocomposite composed of liquid poly (ethylene glycol) diacrylate (PEGDA) and fumed nanosilica (Aerosil R972, Evonik) with different loadings for LCD-SLA 3D printing. Due to the nomenclature, we refer to the cross-linked PEGDA as polyPEGDA. PolyPEGDA is a biocompatible synthetic polymer frequently used in biomedical applications due to its close resemblance to native human tissues and the ability to tune its physical properties [49–51]. PolyPEGDA reveals, however, limited mechanical performance, primarily low elastic modulus, leading to its frequent use in composite forms [43,44,51–56]. The used nanosilica particles are modified with dichlordimethylsilane, and so are anticipated to not aggregate strongly. The resulting 3D printed nanocomposites should effectively bear stress and exhibit high adhesion strength between nanosilica and the polymer matrix, thanks to the high surface-to-volume aspect ratio of the these particles [57].

In this work, we primarily focus on understanding interfacial phenomena, specifically by analysing the contact elastic modulus (hereinafter called Young's modulus) between consecutively printed nanocomposite layers. The interfacial analysis is conducted by Atomic Force Microscopy (AFM) imaging using Quantitative Nanomechanical Mapping (QNM) in PeakForce Tapping mode. Samples are also characterized before (viscosity, polymerization kinetics) and after (glass transition and thermal stability, Fourier-transform infrared spectroscopy, tensile testing) 3D printing. To the best of our knowledge, no data are available in the scientific literature concerning the variation of the mechanical properties across the interface and its vicinity for the 3D printed photopolymer nanocomposites.

2. Experimental

Formulation preparation. The oligomeric PEGDA (M_n 575 g mol^{-1}, Sigma-Aldrich) was stirred with photoinitiator diphenyl(2,4,6-trimethylbenzoyl)phosphine oxide (TPO) (97% purity, Sigma-Aldrich) at 0.5% w/v for 2 h prior the addition of hydrophobic silica nanoparticles (Aerosil R972, Evonik). The Aerosil R972 is a fumed nanosilica, treated with dimethyldichlorosilane that reacts with the silanol groups

at the nanoparticles surface, leading to their moderate hydrophobicity. The average diameter of the nanosilica particles is 16 nm [58] and their specific surface area is 90–130 m^2 g^{-1} [59]. Six mixtures, containing 0, 0.75, 1.5, 3.0 and 6.0% w/v (to the volume of PEGDA) of the nanosilica Aerosil R972 were prepared and stirred over 24–48 h (nanosilica was added in 1 g/100 ml steps to avoid agglomeration). Thereafter, the formulations were homogenized by a sonifier (Branson Digital Sonifier SFX 550) for 10 min (50% power at 20 kHz, 10 s pulsed, 30 s paused) at a controlled temperature (15–20 °C). All formulations were transparent and did not show visual evidence of aggregation. Due to a small difference between refractive indexes of PEGDA and nanosilica no light scattering was observed [60,61].

Viscosity. Viscosities of PEGDA/nanosilica mixtures were measured at the polymerization temperature 25 °C with Digital Viscometer (model DV-II, Canada) in cone-plate geometry at various shear rates.

Polymerization kinetics. Reaction rates were monitored by Differential Scanning Calorimetry (DSC) under isothermal conditions at 25 ± 0.01 °C in a high-purity argon atmosphere (<0.0005% of O$_2$) using the Pyris 6 instrument (Perkin–Elmer, USA) equipped with a lid, specially designed for photochemical measurements. The 2-mg samples were polymerized in open aluminium pans with a diameter 6.6 mm. The polymerizations were initiated by the light from an OmniCure S 1000 high-pressure mercury lamp (OmniCure, England). All DSC photopolymerization experiments were conducted at least in triplicate. For computations, the heat of polymerization was taken to be 86 kJ mol^{-1} per one double bond. Kinetic curves were determined based on steady-state and bimolecular termination assumptions for the photopolymerization of multifunctional monomers [62].

Vat 3D printing. Specimens were printed in a bottom-up configuration from the formulated composition using a Zortrax Inkspire 3D printer (Poland). This printer employs a 405 nm LED source controlled by an LCD screen to cure resins in a layer-by-layer fashion. The formulations were placed in the vat on a tray made of fluorinated ethylene propylene (FEP) foil. Printed samples were modelled using the Z-Suite Zortrax software v.2.20. Ten tensile specimens ASTM-D638 type IV ("dogbones") without supports were printed from each resin composition with a programmed layer thickness (50 μm each, 2300 layers in total). The layer additive direction was set to the longest dimension of "dogbones". The platform speed (up and down) and lift were set to 75 mm min^{-1} and 3 mm, respectively.

The irradiation dosage per printed layer was adjusted using the "Exposure Time Calibration" (ETC) tool in the printer software for a reference resin of pure PEGDA. This approach eliminates the need to establish the so-called Jacob's working curve (the relationship between absorbed UV light energy and the cured thickness of a photopolymer during UV light exposure) to determine the irradiation time/dosage per a 3D printed layer [63]. Using the ETC tool, a model sample with 10 columns, each containing the same features, was printed with varied UV irradiation times for a specific column. The test reveals different curing efficiency in specific columns, including not cured, under-cured, well-cured and over cured features. Visually inspecting the printed columns, the lowest irradiation time that resulted in stable and correct printing of features was chosen as the preferred setting. It our case the irradiation time was found to be 11 s. Since one research goal was to study the effect of nanosilica on the interface between 3D printed layers, the irradiation time of all samples maintained constant. The exception to this rule is the experimental result shown in Fig. 8.

Thermal properties. Glass transition temperature T_g was measured with DSC (Mettler Toledo, Switzerland) under a nitrogen atmosphere at the heating rate of 20 °C min^{-1}. T_g was evaluated from the first and second run DSC measurements at temperature ranges: from −80 °C to 300 °C (the sample was kept 3 min at 0 °C). T_g values are obtained from the midpoint of the step-transition found for each sample.

Thermal stability. The thermal resistance was investigated with a TG 209 F3 Tarsus thermogravimetric analyser (NETZSCH-Geratebau, Germany). Thermogravimetric analysis curves (TGA) and their differentials
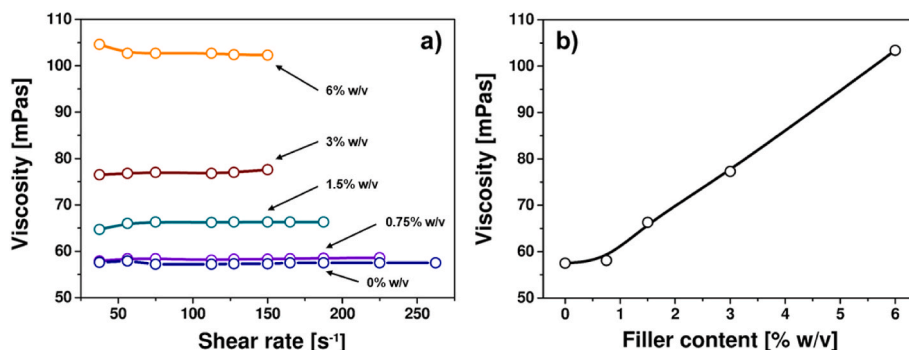
Fig. 1. Viscosity of the formulated resins as a function of (a) the shear rate (the filler content is as indicated) and (b) the filler content. In (b) the viscosity is shown at the shear rate ~150 s^{-1}. The lines are guides for the eye.
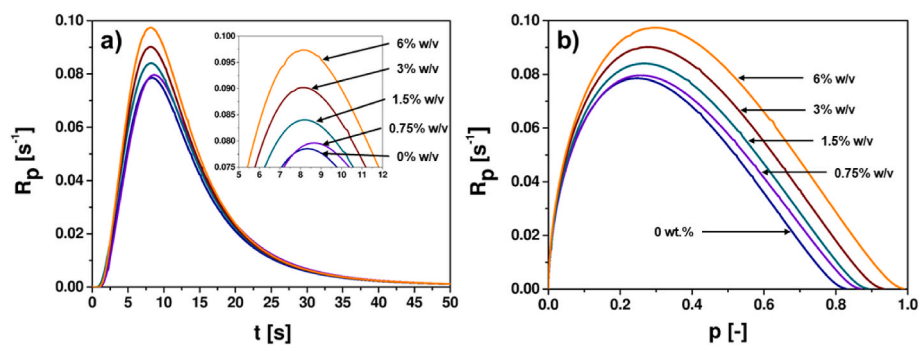

Fig. 2. Polymerization rate (R_p) of the formulated resins as function of (a) the irradiation time (t) and (b) the double bond conversion (p). The filler content is as indicated. The inset in (a) shows the region of the highest polymerization rate in more details.
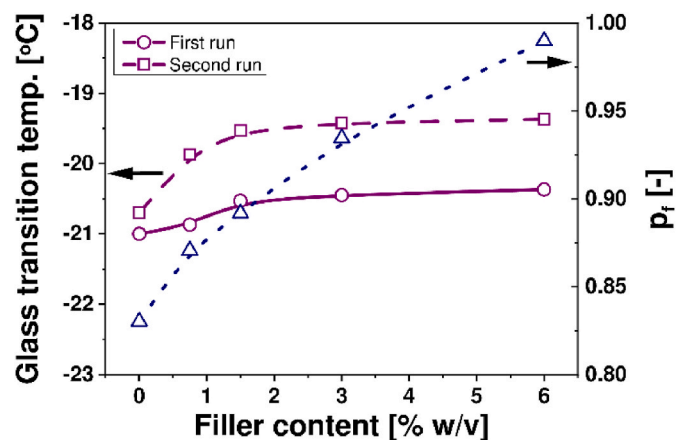

Fig. 3. Glass transition temperature for the first (circles) and second (squares) DSC runs and final double bond conversion p_f (triangles) as a function of the filler content.

Fig. 4. TGA (solid line) and DTG (dashed line) curves of 3D printed samples. The filler content is as indicated.

(DTG) were captured. Samples of 10 mg were heated in Al$_2$O$_3$ crucibles from 40 to 700 °C at a scan rate of 10 °C min^{-1} under a nitrogen atmosphere (a purge of 20 ml min^{-1} of N$_2$ protection gas and 30 mL min^{-1} of N$_2$ sample gas). The decomposition temperature of the material was measured at 10%, 50%, and 90% weight loss. The residual mass (R) was defined at about ~600 °C.

Atomic Force Microscopy. The 3D printed samples in form of "dogbones" (not yet subjected to mechanical tests) were fractured at room temperature to expose their bulk surface. Fractures were made to be perpendicular to the layer additive direction (cross-section of the layers), at random positions along the length of the "dogbone". Quality of the fractured surfaces was checked by optical microscopy (Olympus
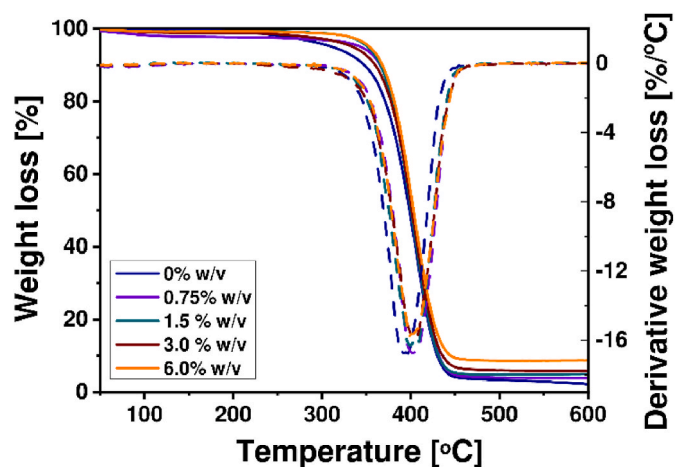
BX60, Japan) prior to AFM imaging of select flat surfaces. A setup with Multimode and NanoScope V controller AFM (Bruker, USA) was used with the JV vertical engage scanner operated in the PeakForce Tapping mode employing the Quantitative Nanomechanical Mapping (PF-QNM). The PF-QNM captures, among others, surface topography and surface stiffness (Young's modulus maps) data. Cantilevers with a nominal spring constant of 2 N m^{-1} and a nominal tip apex radius of 9 nm (OMCL-AC240TS, Olympus, Japan) were used. The sharpness of the tip was assessed through random sample analysis using Scanning Electron Microscopy (SEM) (Fig. S1 in the Supporting Information). The AFM optical sensitivity (deflection sensitivity) was "reverse" calculated using the thermal tune method based on the cantilever spring constant
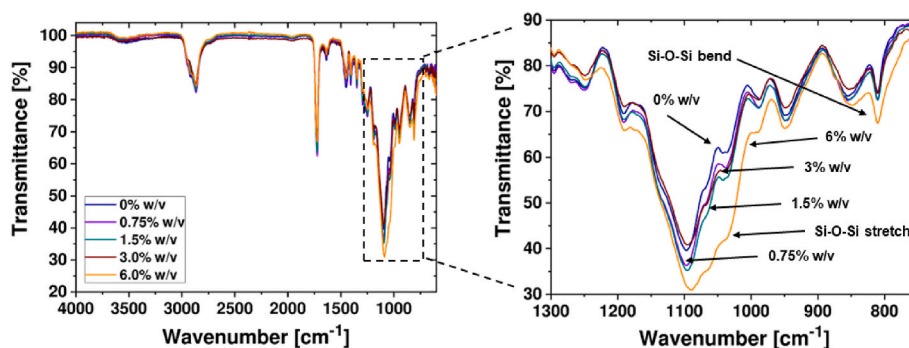
Fig. 5. FTIR spectra recorded for the 3D printed samples. The filler content is as indicated.

nominal values [64]. In the AFM software (NanoScope, version 9.7) the scanning parameters (scan rate, feedback loop, applied load, etc.) were set to "off" to apply dedicated constant values to control stiffness mapping. The data, sampling 512/line (in article) and 256/line (in Supporting Information) force-distance curves, was collected following a sine-wave sample-tip trajectory with a frequency of 2 kHz and utilizing a peak-force amplitude value of 100 nm. The tip was raster-scanned (while vibrating) over the sample surface at speeds less than 10 μm s^{-1}. Measurements were performed in air, at controlled temperatures (21 °C) and relative humidity (~40%). The data analysis was conducted in the NanoScope Analysis software (version 2.0). The cross-section of the surface profiles in Young's modulus maps were smoothed in the OriginPro (ver. 9.0.0) software by the Percentile Filter Method (PFM). The Young's modulus values at the silica nanoparticles (spikes) were treated as the shot noise and processed by the PFM in a way that a value at each point was replaced by the median value of a group of surrounding 50 points.

Two approaches, namely the Derjaguin, Müller, and Toporov (DMT) model of contact mechanics and the "relative modulus determination method" were employed to quantify the surface stiffness [65–67]. The former can be applied for heterogeneous polymer surfaces with low adhesion, and sharp AFM tips; these are characteristics of our system [68,69]. By using the latter, the maximum Young's modulus value observed by AFM for pure polyPEGDA measured across two consecutively printed layer was attributed (brought) to the reference value obtained by tensile testing for pure polyPEGDA (78.7 MPa) by the AFM tip radius value, as the fitting parameter in the NanoScope software. The indentation depth of the AFM tip was kept below 4.5 nm to increase the accuracy of the DMT model. The Poisson's ratio of samples was set to 0.4 as a reasonable estimation for materials that are composed of a mechanically susceptible elastomer and a stiff filer [70].

Fourier-transform infrared (FTIR) spectroscopy. Fourier-transform infrared (FTIR) spectra of the samples were obtained using the attenuated total reflectance (ATR) mode (a Nicolet 5700 equipped with a ZnSe crystal ATR unit, Thermo Fisher Scientific, USA). The spectra were recorded with a resolution of 4 cm^{-1} and an accumulation of 64 spectra.

Tensile testing. Static mechanical properties were characterized by tensile testing on standard ASTM-D638 type IV tensile specimens with a thickness of 4 mm, using an Instron 5565A apparatus (USA) at 50 mm min^{-1} crosshead speed with a 5 kN load cell. As the studied materiel exhibits brittle characteristics, values of Young's modulus (fitting: from 0.2 to 0.8% deformation), tensile stress at break, and elongation at break were calculated. Eight samples per a type were tested and results averaged. To compare statistically the differences of mean, the analysis of variance (ANOVA statistics in OriginPro 2021b software) using the Tukey test at a significant level of p < 0.05 was performed.

3. Results and discussion

### 3.1. Characterization of the dispersion of nanosilica in PEGDA

Viscosity (η) measurements are essential in studying 3D-printing resin primarily because the fluid mechanics must be adapted to the movements of the printer platform [32]. Preferentially, photosensitive resins should have low viscosity and good fluidity which enables self-levelling of layers. Viscosity of the resin is an important parameter to ensure good quality of 3D-printed objects and can affect the rate of photopolymerization. Primarily, the termination reactions in the resins are diffusion controlled, and those depend on the viscosity of the reaction medium.

The viscosity of both the pure PEGDA and its formulation with nanosilica exhibited near Newtonian behaviour and rather low absolute value (Fig. 1). Newtonian behaviour is also an important feature as the formulations can be used with various 3D printers (small and large vat) and at different platform speeds. Addition of silica nanoparticles increased the viscosity compared to pure PEGDA, however, even at the maximum studied loading (6% w/v) the viscosity value is only doubled, thus not hindering 3D printability. In all samples, 30% of the silanol groups are converted to Si-O-Si-(CH$_3$)$_2$ units [71]. The remaining silanol groups can still interact via hydrogen bonding, thus increase the viscosity.

The dependence of the polymerization rate R_p on the irradiation time t (Fig. 2a) and double bonds conversion p (Fig. 2b) for formulations with different silica contents show an immediate onset of autoacceleration and occurrence of a maximum polymerization rate R_p^{max}. These phenomena are typical for the free-radical polymerization of acrylates with fillers [54,72,73]. In our study, the addition of the silica to the PEGDA affects the reaction kinetics. We generally observe an enhancement of the gel effect (a reduction of the induction period, an increase in R_p and R_p^{max}). The amount of filler (1.5–6% w/v) added notably accelerates the crosslinking reaction (see inset in Fig. 2a). Slowing down the diffusion of macroradicals (viscosity increase), resulting in suppressed termination of the photopolymerization process, and, in a consequence, an accelerated crosslinking. The same trend is observed for final degree (p_f) of conversion (Fig. 3): compositions (filler containing >1.5% w/v) are the most reactive and have a positive effect on photopolymerization process and, consequently, the 3D printing procedure. The maximum polymerization rate Rp^{max} appears in the range of 25–35% of double bond conversion.

3.2. Characterization of the 3D printed samples

Complex interrelationships, including filler type, cross-link density, material heterogeneity, and curing conditions affect the glass transition temperature, T_g, in photopolymer composites. Our unfilled polymer, polyPEGDA, is an elastomeric material that has a glass transition temperature lower than room temperature ($T_g \sim -21$ °C) (Fig. 3). The
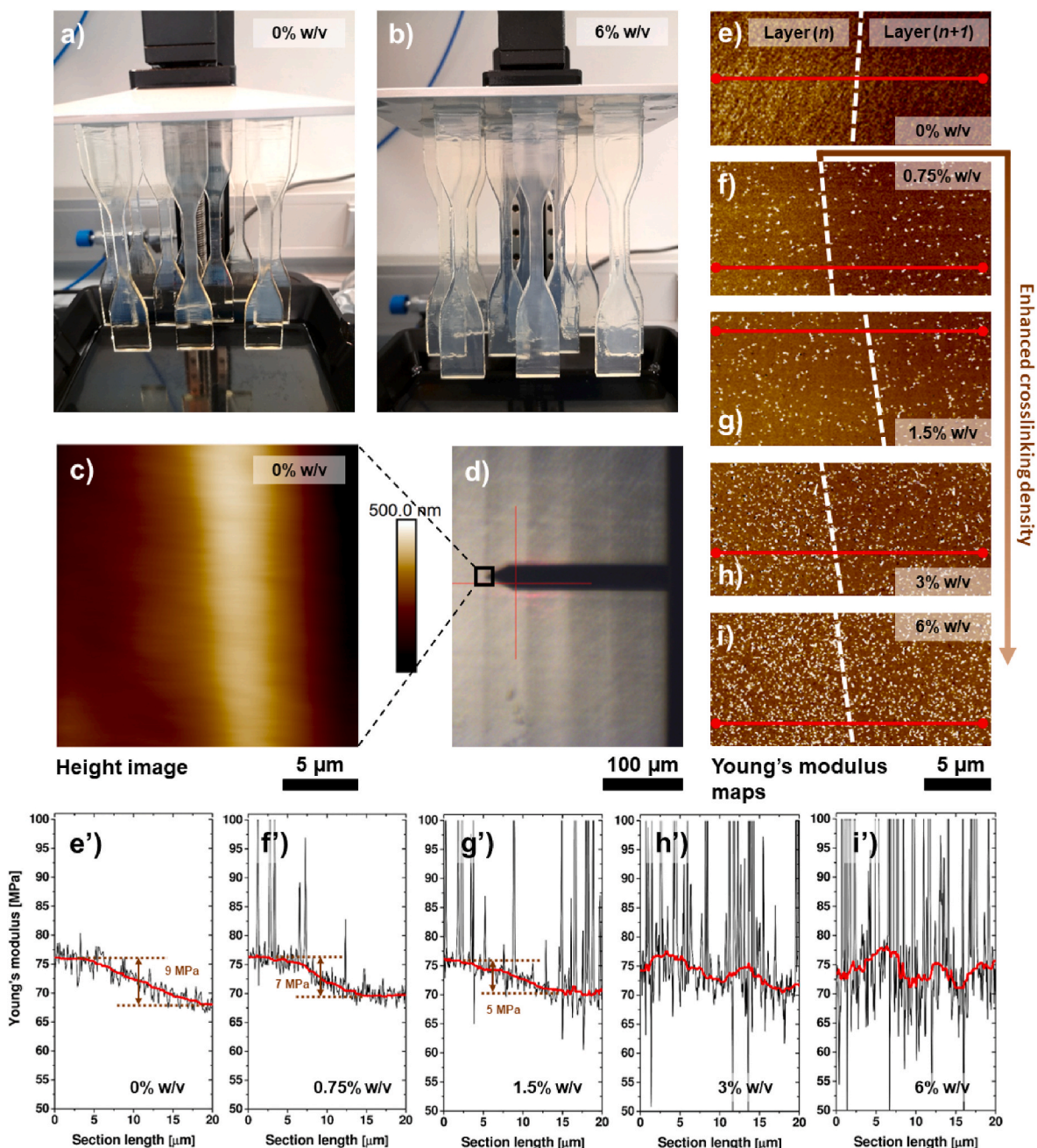
Fig. 6. Results of 3D printing. Photos show the printed dogbones (each 115 cm length) of (a) pure polyPEGDA and (b) polyPEGDA with 6% w/v of the nanosilica filler. AFM height image (c) is captured for the selected area indicated by a black square in (d) the optical microscopy image (fractured surface of pure polyPEGDA). Young's modulus maps (e-i) are captured at two consecutively printed layers (at the interface and its vicinity) for pure polyPEGDA and its nanocomposites (content as indicated). The colour code: bright – stiffer, darker – softer. The borderline (white, dashed) represents a geometrical boundary at which the layer (n) starts to be cured, as the first, and the layer ($n + 1$) is completed and attached to the layer (n), as the next. Note that the borderlines position is approximate. The images pixel size is 59 nm × 59 nm. Cross-section Young's modulus profiles (e'-I') refer to the section lines shown on the maps (e-i) in red. The cross-sections were smoothed by Percentile Filter Method to remove trace peaks related to nanosilica (red curve). The orange dashed lines (e'-g') represent the highest (layer n) and lowest (layer $n +$ 1) values of the Young's modulus; their differences are indicated.

addition of nanosilica notably increases the T_g at loading of 0.75 and 1.5% w/v, while at higher loadings (3.0 and 6.0% w/v), the increase is slightly. Nanosilica particles (topological constraints) influence the mobility of polymer segments, especially chains near the particle surface. Hence, an increase in T_g after adding silica is observed.

TGA proved that the 3D printed materials were stable up to 300 °C (Fig. 4). At temperatures between 300 and 330 °C, degradation started. Single stage decomposition of all samples occurred at approx. 400 °C as visible at differential thermogravimetric analysis (DTA) curves.

Composites containing nanosilica showed slightly higher thermal stability than pure matrix, especially in the temperature range of 300–400 °C, which can be attributed to the good interaction between silica and polymer. Such thermal stability-enhancing behaviour could be also explained by the lower surface energy of silica particles, providing thermal insulation to the matrix at high temperature [74]. Residual masses of polymer nanocomposite after the heating process increased above the silica content in the materials, suggesting that the fillers also influence the overall material decomposition pathway. Relevant TGA
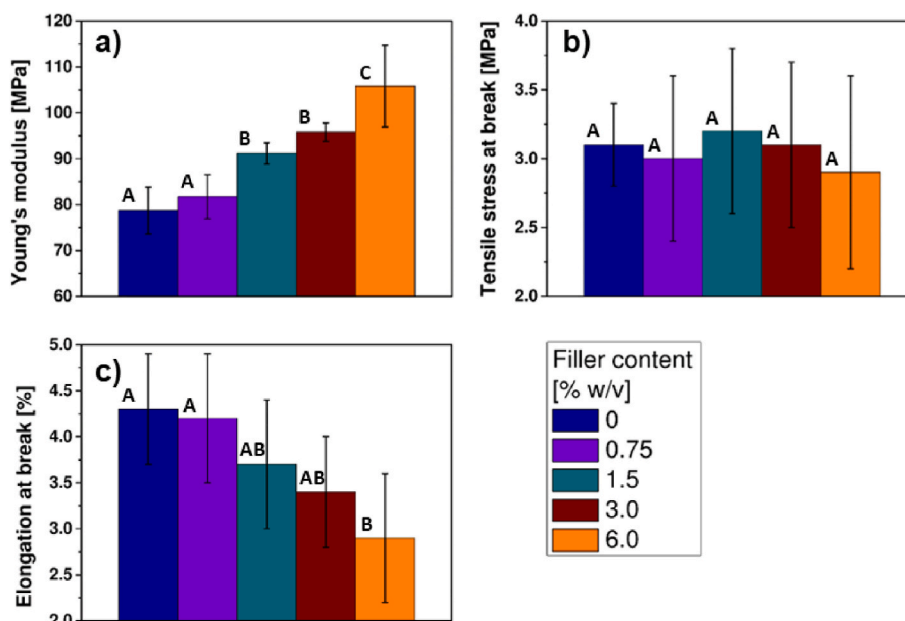
Fig. 7. (a) Young's modulus, (b) tensile stress at break and (c) elongation at break values obtained in static mechanical testing (tensile) for 3D printed samples. Error bars represent standard deviation. Capital letters indicate results of Tukey analysis (ANOVA test); means that do not share a letter are significantly different. The nanosilica content is as indicated.

Fig. 8. Photos of the 3D printed fullerene buckyballs at 8 s of the irradiation time using: a) pure polyPEGDA and b) polyPEGDA composition with 6.0% w/v nanosilica. The size of structures is 32 mm.

parameters are gathered in Table S1 (Supporting Information).

We additionally studied the presence of polymer-nanosilica interactions by observation of absorption bond shifts for characteristic groups in FTIR spectra (Fig. 5). On the spectrum of a polymer matrix the peaks located at values of 2860–3000 cm^{-1} correspond to the C–H stretching vibrations, whereas the band at 854 cm^{-1} represents C–H bending group. The band centred at 1349 cm^{-1} and 1250 cm^{-1} are attributed to C–O asymmetric bending, whereas peaks at 1093 cm^{-1} and 948 cm^{-1} assigned to C–O–C stretching. The peak at 1723 cm^{-1} is observed due to the frequency of the C=O stretching. According to the literature [75], the carbonyl band should occur at wave number ~ 1720 cm^{-1}, and its shift towards a higher wavelength number (from 1720 cm^{-1}–1730 cm^{-1}) indicates crosslinking of the monomer.

The FTIR spectra of composites also showed absorption bands at ~810 cm^{-1} and ~1100 cm^{-1}. The band at 1090 cm^{-1} corresponds to the asymmetric stretching vibration of Si-O-Si groups, while the peak at 810 cm^{-1} can be attributed to the symmetric deformation of the Si-O-Si bonds. These bands (1090-1100 cm^{-1}) shift towards shorter wavenumbers and become broader with increasing filler content in the matrix, indicating emerging interactions in the polymer nanocomposite. These bands are also the broadest for printed polymer composites

containing 6 % w/v silica, indicating efficient interactions between matrix and fillers. In all 3D printed samples there is a small characteristic band at ~1635 cm^{-1} coming from the –C=C group's stretching, indicating an incomplete polymerization reaction. This is, however, specific and needed in 3D printed photopolymer materials for stable joints between the layers [11]. The absorption peaks between 3200 and 3600 cm^{-1} characterise O–H stretch vibrations is small and is due to presence of small amounts of moisture.

In the second to last part, we examine the AFM Young's modulus maps of the fractured 3D printed samples (Fig. 6a and b) and tensile tests (Fig. 7). An area of our interest i.e., interface and its vicinity, is first selected using optical microscopy (Fig. 6d), then characterized by quantitative AFM imaging (Fig. 6c). Unlike the 3D printed nanocomposites, the reference sample (pure polyPEGDA) reveals a noticeably wavy surface profile in AFM height images at the interface (Fig. 6c). This surface profile resulted from the sample fracturing. The crack propagates "along" the variation of crosslinking density [11,76].

All samples tested were 3D printed correctly in their entirety. For fractured surfaces both AFM imaging and optical microscopy (Figs. S2 and S3 in the Supporting Information) indicated no evidence of solid nanosilica aggregation. Nevertheless, the opaque character of the

sample gets more intense with the increasing nanosilica loading (compare Fig. 6a and b and see Fig. S4 in the Supporting Information). We attribute it to a difference between the refractive indexes of the components i.e., for nanosilica around 1.46, and for polyPEGDA around 1.51 [60,61]. As no match between them exists in the final material, the light interferes (scatters) with the nanoparticles causing its limited transmittance though the samples. Also, the higher the nanosilica loading the higher the light scattering.

The AFM Young's modulus maps expose the bulk surface of the interface and its vicinity (Fig. 6e–i). The horizontal size of the maps, approximately 20 μm, is optimal for observing and analyzing both the interface and the distribution of nanosilica. In the reference sample (3D-printed pure polyPEGDA), the stiffness decays across individual layers, which is rationalized by variations in light absorption within the matter (Fig. 6e and e'). Depending on the material used for the light penetration window in the vat and the complexity of a resin (including the diffusive properties of the crosslinkable molecules and photoinitiator), the interface can unveil multiple individual regions. For instance, in our recent studies, we demonstrated that using the light penetration window made of polydimethylsiloxane (PDMS)-covered glass results in the occurrence of two regions in the interface [11]. The two region-interface is a consequence of heterogeneities of the photopolymerization i.e., molecular diffusion across the interface (transition region) and atmospheric oxygen inhibition (inhibition region). In the latter, the oxygen is released from the PDMS (as it can highly concentrate and "reoxygenate" the oxygen collected from the resin). Contrary to that, in this study the FEP foil is used in the vat, thus oxygen inhibition of the photopolymerization does not occur (FEP can barely concentrate oxygen) and the interfacial region related to the inhibition process is not observed in the AFM maps [11,77–79]. Nevertheless, the transition region in vat photopolymer 3D printing always appears, except for some 3D printing modifications that exclude the layer-by-layer processing, like the CLIP technology (Continuous Liquid Interface Production) [27], or when it is limited by the printer modifications [80]. In most cases, including our own, the transition region occurs because the resin comes into contact with the layer, and the unreacted double bonds of the layer act as bridging sites. Additionally, both the matrix and photoinitiator molecules can diffuse across the interlayer joints. The PEGDA molecular diffusion shows a "fuzzy" transition region with no sharp borderline between the consecutively printed layers (compare n and $n + 1$ layers in Fig. 6e and e'). It was reported that PEGDA network can be diffused even by large molecules, thus diffusion of oligomeric (uncured) PEGDA through the cured polyPEGDA may be considered in our work as well [81].

The bright spots in the AFM Young's modulus maps indicate nanosilica particles. (Nano)silica is much stiffer than the elastomeric polyPEGDA, thus AFM cross-section plots show significant data scattering. In order to study the elasticity of the matrix only, the cross-section data was "smoothed" by the PFM (see Experimental part), resulting in removing data associated with the nanosilica particles (red curve in Fig. 6f'-6i'). At the low nanosilica loading i.e., 0.75% w/v, the Young's modulus data exhibits a decay, similarly to unfilled 3D printed polyPEGDA samples (Fig. 6e' vs Fig. 6f'), but the relative difference between the highest (layer n) and lowest (layer $n + 1$) Young's modulus values tends to be reduced (9 vs. 7 MPa). This difference decreases with increasing nanosilica content i.e., 1.5, 3.0 and 6.0% w/v, which we translate to layer stiffening by improved cross-linking density of the polyPEGDA matrix. For high nanosilica loadings (3.0 and 6.0% w/v), determining the relative difference between the highest (layer n) and lowest (layer $n + 1$) Young's modulus values proved challenging due to increased nanosilica surface density (variation in AFM cross-section data). Nonetheless, a clear trend is evident in all Young's modulus maps: the colour contrast in the maps gradually becomes consistent for both layers, n and $n + 1$; at the nanosilica loading of 6.0 % w/v it becomes unnoticeable.

On this point, one potential effect should be discussed. Namely, the interaction volume of the AFM indentation mapping in respect of the possibility to interfacial stiffening by underlying or neighbouring nanosilica, and thus to influence the monitored (surface) Young's modulus values [55]. Nanosilica can be a "rigid wall" for the polymer matrix and therefore locally give a contribution to the increase in the value of Young's modulus measured by the AFM. Brune et al. through the analysis of AFM data collected from surfaces consisting of covalently attached rubber films on silicon wafers, estimated an interfacial thickness of approximately 50 nm [82]. Within this thickness, the stiffness gradually increased from the value for rubber to that for silicon wafer. Comparable interfacial thicknesses were reported by Song et al. for similar system i.e., poly (methyl methacrylate) at rigid infinite wall [83]. Our nanosilica, however, cannot be equated with an infinite wall, as it only plays the role of dispersed inclusions. Thus, the polymer stress field cannot be accumulated during the indentation mapping. Moreover, even for the highest loading of nanosilica, the distance between the inclusions is much greater than 50 nm (Fig. S3 in the Supporting Information). The distances between inclusions are then sufficient for polymer stress field to be unperturbed [84]. Given the above, we believe that the effect of interfacial stiffening of the polymer matrix by nanosilica is at most small in our case. Therefore, the explanation for the observation of AFM results should be moved to another direction.

To that end, the increase of the formulation viscosity is suggested by us as a factor to be considered for the evolution of the properties at the interface and within the layers. However, nanosilica was also reported to accelerate the curing kinetics during radical polymerization [85]. We think that due to the high specific surface area of nanosilica particles, our system can find a new path to initiate more chain propagation (the specific surface area of the nanosilica used is high, up to 130 m^2 g^{-1}) [86]. Additionally, throughout polymerization, interactions between the filler surface and the polymer chains change the mobility of the polymer segments by forming an interfacial region; possible hydrogen bonding between the polymer chains and the silica can also affect the curing kinetics by changing the mobility of macroradicals and monomer particles. Growing macroradicals are immobilised on the silica surface, which can enhance suppression of termination (macroradicals react less with each other to terminate polymerization), however monomer molecules diffuse faster, leading to higher reaction rates [85]. The accelerated photopolymerization is confirmed by our kinetic studies: the polymerization rate (Fig. 2) and the final double bond conversion (Fig. 3) are both the highest at the maximum nanosilica loading. Additionally, the FTIR analysis indicates good matrix-nanosilica interactions, especially at 6.0% w/v of the loading (Fig. 5).

The evolution of the crosslinking density can also be appreciated by analysis of the tensile testing results (Fig. 7). Although the stress at break remains rather constant (see Tukey analysis; ANOVA test), the macroscopic Young's modulus increased once the nanosilica is added to the matrix. At maximum loading of polymer matrix with nanoparticles, the Young's modulus increases by approximately 25% compared to pure polymer, while the elongation at break decreased by approximately 45%. This is expected and typical in polymer nanocomposites [86]. One should keep in mind that the load was applied perpendicular to the interfaces (along with "dogbones"), such that they contribute to the mechanical data. Therefore, the bulk mechanical behaviour will attribute to the enhanced stiffness of the interfaces (and vicinities) as well, but also to their increased susceptibility to brittleness.

The last point to discuss here is the UV light scattering during curing of the 3D printed layers. When fillers of a different refractive index are added to a matrix, the light interferes with the particles (scatter) [60]. Because the filler size and its dispersed inclusions (Fig. S3 in the Supporting Information) are smaller than the light wavelength, in our case, the light scattering occurs in all directions and is described by the Rayleigh theory. Uncured and cured PEGDA have refractive indexes of 1.47 and 1.51, respectively, while nanosilica – 1.47, at the 3D printer working wavelength of 405 nm [61,87]. Since the starting composition holds almost a refractive index match, the light is not anticipated to scatter. During the printing process, light progressively scatters as

PEGDA undergoes changes in its refractive index during curing. However, as light scattering increases, curing depth decreases (the curing depth of nanocomposites is inversely proportional to the square difference of refractive index between the matrix and the nanoparticles [88]). As the incorporation of nanoparticles in the matrix increases, the "contrast" between these opposing effects becomes stronger. However, since light intensity attenuates exponentially within the sample (layer), enhanced light scattering dominantes. Furthermore, with higher loadings, one can also expect multiple scattering (at many particles/inclusions by the same ray) because of the small distance between particles or inclusions [89]. These considerations lead us to the conclusion that adding nanosilica to the polymeric matrix of 3D printed samples increases the stiffness of the polymer interfacial area and its vicinity through the enhanced light scattering.

To finally prove our discussion conclusions, we performed a 3D printing test by manufacturing fullerene buckyball samples. The pure polyPEGDA (Fig. 8a) and its composition with 6.0% w/v nanosilica (Fig. 8b) are 3D printed using the same printing parameters as the other samples studied here, but at different irradiation time to be set at 8 s. Eight second of the irradiation time was found a minimum for the composite sample to be printed without defects, however it remains too little for the pure polyPEGDA, resulting in fragmented printing with thinner arms. This confirms our findings about improved crosslinking density of the matrix, thus its stiffening at the interface and its vicinity by nanosilica. This also evidences that loading the matrix with silica nanoparticles can reduce the overall printing time.

4. Summary

Within this study, we directly observed that adding nanosilica particles (Aerosil R972, Evonik) to multifunctional liquid PEGDA reinforces the interface area and its vicinity by higher crosslinking density in 3D printed samples. Quantitative AFM analysis shows that the stiffness (Young's modulus value) decays within the layers, which is rationalized by the variation in light absorbed for each layer. The relative variation of the AFM Young's modulus values across the interface and its vicinity is reduced when nanosilica is added to the polymeric matrix. The difference between the AFM Young's modulus values across the polymer matrix within the 3D printed layer is close to zero when 6.0% w/v of nanosilica is added. This reduces the microscopic inhomogeneity of the 3D printed samples, resulting in more bulk properties. We suggested two processes involved in this observation: (i) the increase of the viscosity by nanosilica that leads to indirect acceleration of the crosslinking in the matrix and (ii) the increase of the light scattering by nanosilica that results in directly enhanced crosslinking of the matrix. We also show that by adding the silica nanoparticles the overall polymerization can be speeded up, hence reducing the overall time needed for 3D printing. In our study, pure PEGDA needed 11 s to be layer-cured, while with 6% w/v nanosilica added the time was reduced to 8 s. We also noted that already at 3% w/v of the nanosilica loading, one can appreciate an enhanced crosslinking density at the interface and its vicinity, with bulk mechanical properties to be compromised i.e., limited elongation at break.

We believe that incorporation of nanosilica particles to other acrylic resins can potentially bring the same effect of enhanced interfacial layer binding. Hence, this simple approach can be competitive to other technological modifications of vat photopolymer 3D printing, like CLIP or defocusing of the image pattern in LCD-SLA printers [27,80].

Data availability

Data will be made available on request.

Acknowledgements

Appendix A. Supplementary data

Supplementary data to this article can be found online at https://doi.org/10.1016/j.polymertesting.2023.108243.

References

[1] I. Gibson, D. Rosen, B. Stucker, M. Khorasani, Additive Manufacturing Technologies, third ed., Springer International Publishing, 2021.

[2] T.D. Ngo, A. Kashani, G. Imbalzano, K.T.Q. Nguyen, D. Hui, Additive manufacturing (3D printing): a review of materials, methods, applications and challenges, Compos. B Eng. 143 (2018) 172–196.

[3] B.C. Gross, J.L. Erkal, S.Y. Lockwood, C. Chen, D.M. Spence, Evaluation of 3D printing and its potential impact on biotechnology and the chemical sciences, Anal. Chem. 86 (7) (2014) 3240–3253.

[4] S.C. Ligon, R. Liska, J. Stampfl, M. Gurr, R. Mülhaupt, Polymers for 3D printing and customized additive manufacturing, Chem. Rev. 117 (15) (2017) 10212–10290.

[5] M. Gebler, A.J.M. Schoot Uiterkamp, C. Visser, A global sustainability perspective on 3D printing technologies, Energy Pol. 74 (C) (2014) 158–167.

[6] V.A. Bobrin, K. Lee, J. Zhang, N. Corrigan, C. Boyer, Nanostructure control in 3D printed materials, Adv. Mater. 34 (4) (2022).

[7] V.S.D. Voet, J. Guit, K. Loos, Sustainable photopolymers in 3D printing: a review on biobased, biodegradable, and recyclable alternatives, Macromol. Rapid Commun. 42 (3) (2021), 2000475.

[8] P. Urhal, A. Weightman, C. Diver, P. Bartolo, Robot assisted additive manufacturing: a review, Robot. Comput. Integrated Manuf. 59 (2019) 335–345.

[9] Z. Zhu, D.W.H. Ng, H.S. Park, M.C. McAlpine, 3D-printed multifunctional materials enabled by artificial-intelligence-assisted fabrication technologies, Nat. Rev. Mater. 6 (1) (2021) 27–47.

[10] L. Zorzetto, L. Andena, F. Briatico-Vangosa, L. De Noni, J.M. Thomassin, C. Jérôme, et al., Properties and role of interfaces in multimaterial 3D printed composites, Sci. Rep. 10 (1) (2020).

[11] H. Gojzewski, Z. Guo, W. Grzelachowska, M.G. Ridwan, M.A. Hempenius, D. W. Grijpma, et al., Layer-by-Layer printing of photopolymers in 3D: how weak is the interface? ACS Appl. Mater. Interfaces 12 (7) (2020) 8908–8914.

[12] N.P. Levenhagen, M.D. Dadmun, Improving interlayer adhesion in 3D printing with surface segregating additives: improving the isotropy of acrylonitrile-butadiene-styrene parts, ACS Appl. Polym. Mater. 1 (4) (2019) 876–884.

[13] N.D. Dolinski, E.B. Callaway, C.S. Sample, L.F. Gockowski, R. Chavez, Z.A. Page, et al., Tough multimaterial interfaces through wavelength-selective 3D printing, ACS Appl. Mater. Interfaces 13 (18) (2021) 22065–22072.

[14] N. Aliheidari, R. Tripuraneni, A. Ameli, S. Nadimpalli, Fracture resistance measurement of fused deposition modeling 3D printed polymers, Polym. Test. 60 (2017) 94–101.

[15] F. Peng, Z. Zhao, X. Xia, M. Cakmak, B.D. Vogt, Enhanced impact resistance of three-dimensional-printed parts with structured filaments, ACS Appl. Mater. Interfaces 10 (18) (2018) 16087–16094.

[16] N.P. Levenhagen, M.D. Dadmun, Bimodal molecular weight samples improve the isotropy of 3D printed polymeric samples, Polymer 122 (2017) 232–241.

[17] A. Tofangchi, P. Han, J. Izquierdo, A. Iyengar, K. Hsu, Effect of ultrasonic vibration on interlayer adhesion in Fused Filament Fabrication 3D printed ABS, Polymers 11 (2) (2019).

[18] G. Zhu, Y. Hou, J. Xu, N. Zhao, Digital light processing 3D printing of enhanced polymers via interlayer welding, Macromol. Rapid Commun. 43 (9) (2022).

[19] Q. Ge, A.H. Sakhaei, H. Lee, C.K. Dunn, N.X. Fang, M.L. Dunn, Multimaterial 4D printing with tailorable shape memory polymers, Sci. Rep. 6 (2016).

[20] Y.Y.C. Choong, S. Maleksaeedi, H. Eng, S. Yu, J. Wei, P.C. Su, High speed 4D printing of shape memory polymers with nanosilica, Appl. Mater. Today 18 (2020), 100515.

[21] X. Shi, V.A. Bobrin, Y. Yao, J. Zhang, N. Corrigan, C. Boyer, Designing nanostructured 3D printed materials by controlling macromolecular architecture, Angew. Chem., Int. Ed. 61 (35) (2022).

[22] N. Corrigan, C. Boyer, 3D printing and in situ surface modification via type I photoinitiated reversible addition-fragmentation chain transfer polymerization, J. Vis. Exp. 2022 (180) (2022).

[23] A.R. Torrado Perez, D.A. Roberson, R.B. Wicker, Fracture surface analysis of 3D-printed tensile specimens of novel ABS-based materials, J. Fail. Anal. Prev. 14 (3) (2014) 343–353.

[24] M.A. Caminero, J.M. Chacón, I. García-Moreno, J.M. Reverte, Interlaminar bonding performance of 3D printed continuous fibre reinforced thermoplastic composites using fused deposition modelling, Polym. Test. 68 (2018) 415–423.

[25] Y. Tao, F. Kong, Z. Li, J. Zhang, X. Zhao, Q. Yin, et al., A review on voids of 3D printed parts by fused filament fabrication, J. Mater. Res. Technol. 15 (2021) 4860–4879.

[26] J.M. Chacón, M.A. Caminero, E. García-Plaza, P.J. Núñez, Additive manufacturing of PLA structures using fused deposition modelling: effect of process parameters on mechanical properties and their optimal selection, Mater. Des. 124 (2017) 143–157.

[27] J.R. Tumbleston, D. Shirvanyants, N. Ermoshkin, R. Janusziewicz, A.R. Johnson, D. Kelly, et al., Continuous liquid interface production of 3D objects, Science 347 (6228) (2015) 1349–1352.

[28] J. Allum, A. Moetazedian, A. Gleadall, V.V. Silberschmidt, Interlayer bonding has bulk-material strength in extrusion additive manufacturing: new understanding of anisotropy, Addit. Manuf. (2020) 34.

[29] Z. Zhao, D. Wu, H.S. Chen, H. Jerry Qi, D. Fang, Indentation experiments and simulations of nonuniformly photocrosslinked polymers in 3D printed structures, Addit. Manuf. 35 (2020).

[30] A. Bagheri, J. Jin, Photopolymerization in 3D printing, ACS Appl. Polym. Mater. 1 (4) (2019) 593–611.

[31] A. Andreu, P.C. Su, J.H. Kim, C. Siang, S. Kim, I. Kim, et al., 4D printing materials for vat photopolymerization, Addit. Manuf. (2021) 44.

[32] H. Quan, T. Zhang, H. Xu, S. Luo, J. Nie, X. Zhu, Photo-curing 3D printing technique and its challenges, Bioact. Mater. 5 (1) (2020) 110–115.

[33] W. Zhu, X. Ma, M. Gou, D. Mei, K. Zhang, S. Chen, 3D printing of functional biomaterials for tissue engineering, Curr. Opin. Biotechnol. 40 (2016) 103–112.

[34] H. Hong, Y.B. Seo, D.Y. Kim, J.S. Lee, Y.J. Lee, H. Lee, et al., Digital light processing 3D printed silk fibroin hydrogel for cartilage tissue engineering, Biomaterials (2020) 232.

[35] W. Shan, Y. Chen, M. Hu, S. Qin, P. Liu, 4D printing of shape memory polymer via liquid crystal display (LCD) stereolithographic 3D printing, Mater. Res. Express 7 (10) (2020).

[36] D.K. Patel, A.H. Sakhaei, M. Layani, B. Zhang, Q. Ge, S. Magdassi, Highly stretchable and UV curable elastomers for digital light processing based 3D printing, Adv. Mater. 29 (15) (2017).

[37] B. Zhang, H. Li, J. Cheng, H. Ye, A.H. Sakhaei, C. Yuan, et al., Mechanically robust and UV-curable shape-memory polymers for digital light processing based 4D printing, Adv. Mater. 33 (27) (2021).

[38] N.P. Macdonald, J.M. Cabot, P. Smejkal, R.M. Guijt, B. Paull, M.C. Breadmore, Comparing microfluidic performance of three-dimensional (3D) printing platforms, Anal. Chem. 89 (7) (2017) 3858–3866.

[39] Q. Mu, L. Wang, C.K. Dunn, X. Kuang, F. Duan, Z. Zhang, et al., Digital light processing 3D printing of conductive complex structures, Addit. Manuf. 18 (2017) 74–83.

[40] X. Wang, M. Jiang, Z. Zhou, J. Gou, D. Hui, 3D printing of polymer matrix composites: a review and prospective, Compos. B Eng. 110 (2017) 442–458.

[41] U. Kalsoom, P.N. Nesterenko, B. Paull, Recent developments in 3D printable composite materials, RSC Adv. 6 (65) (2016) 60355–60371.

[42] V.C.F. Li, X. Kuang, A. Mulyadi, C.M. Hamel, Y. Deng, H.J. Qi, 3D printed cellulose nanocrystal composites through digital light processing, Cellulose 26 (6) (2019) 3973–3985.

[43] A. Tang, J. Li, J. Li, S. Zhao, W. Liu, T. Liu, et al., Nanocellulose/PEGDA aerogel scaffolds with tunable modulus prepared by stereolithography for three-dimensional cell culture, J. Biomater. Sci. Polym. Ed. 30 (10) (2019) 797–814.

[44] N.B. Palaganas, J.D. Mangadlao, A.C.C. De Leon, J.O. Palaganas, K.D. Pangilinan, Y.J. Lee, et al., 3D printing of photocurable cellulose nanocrystal composite for fabrication of complex architectures via stereolithography, ACS Appl. Mater. Interfaces 9 (39) (2017) 34314–34324.

[45] A. Ji, S. Zhang, S. Bhagia, C.G. Yoo, A.J. Ragauskas, 3D printing of biomass-derived composites: application and characterization approaches, RSC Adv. 10 (37) (2020) 21698–21723.

[46] C.I. Higgins, T.E. Brown, J.P. Killgore, Digital light processing in a hybrid atomic force microscope: in Situ, nanoscale characterization of the printing process, Addit. Manuf. 38 (2021).

[47] C.I. Higgins, T.E. Brown, J.P. Killgore, Digital light processing in a hybrid atomic force microscope: in Situ, nanoscale characterization of the printing process, Addit. Manuf. 38 (2021), 101744.

[48] C. Hofstetter, S. Orman, S. Baudis, J. Stampfl, Combining cure depth and cure degree, a new way to fully characterize novel photopolymers, Addit. Manuf. 24 (2018) 166–172.

[49] S. Nemir, H.N. Hayenga, J.L. West, PEGDA hydrogels with patterned elasticity: novel tools for the study of cell response to substrate rigidity, Biotechnol. Bioeng. 105 (3) (2010) 636–644.

[50] S.J. Lee, W. Zhu, M. Nowicki, G. Lee, D.N. Heo, J. Kim, et al., 3D printing nano conductive multi-walled carbon nanotube scaffolds for nerve regeneration, J. Neural. Eng. 15 (1) (2018).

[51] B. Zhang, S. Li, H. Hingorani, A. Serjouei, L. Larush, A.A. Pawar, et al., Highly stretchable hydrogels for UV curing based high-resolution multimaterial 3D printing, J. Mater. Chem. B 6 (20) (2018) 3246–3253.

[52] X. Zhai, C. Hou, H. Pan, W.W. Lu, W. Liu, C. Ruan, Nanoclay incorporated polyethylene-glycol nanocomposite hydrogels for stimulating in vitro and in vivo osteogenesis, J. Biomed. Nanotechnol. 14 (4) (2018) 662–674.

[53] S. Mishra, F.J. Scarano, P. Calvert, Rapid prototyping of three-dimensional nanocomposite hydrogel constructs: effect of silica nanofiller on swelling and solute release behaviors of the nanocomposite hydrogels, J. Biomed. Mater. Res. 103 (10) (2015) 3237–3249.

[54] M. Sadej, E. Andrzejewska, Silica/aluminum oxide hybrid as a filler for photocurable composites, Prog. Org. Coating 94 (2016) 1–8.

[55] H. Gojzewski, M. Sadej, E. Andrzejewska, M. Kokowska, Nanoscale Young's modulus and surface morphology in photocurable polyacrylate/nanosilica composites, Eur. Polym. J. 88 (2017) 205–220.

[56] A. Chiappone, E. Fantino, I. Roppolo, M. Lorusso, D. Manfredi, P. Fino, et al., 3D printed PEG-based hybrid nanocomposites obtained by sol-gel technique, ACS Appl. Mater. Interfaces 8 (8) (2016) 5627–5633.

[57] H.I. Hsiang, Y.L. Chang, C.Y. Chen, F.S. Yen, Silane functional effects on the rheology and abrasion resistance of transparent SiO2/UV-curable resin nano-composites, Mater. Chem. Phys. 120 (2–3) (2010) 476–479.

[58] V. Karde, S. Panda, C. Ghoroi, Surface modification to improve powder bulk behavior under humid conditions, Powder Technol. 278 (2015) 181–188.

[59] Evonik. Aerosil R972 product data sheet (https://www.productcenter.coating-additives.com/pdf/daten/engl/AEROSIL_R_972.pdf)..

[60] J. Loste, J.M. Lopez-Cuesta, L. Billon, H. Garay, M. Save, Transparent polymer nanocomposites: an overview on their synthesis and advanced properties, Prog. Polym. Sci. 89 (2019) 133–158.

[61] H. Takahashi, T. Kan, G. Lee, N. Dönmez, J. Kim, J. Park, et al., Self-focusing 3D lithography with varying refractive index polyethylene glycol diacrylate, APEX 13 (7) (2020).

[62] E. Andrzejewska, Photopolymerization kinetics of multifunctional monomers, Prog. Polym. Sci. 26 (4) (2001) 605–665.

[63] P.F. Jacobs, D.T. Reid, Rapid Prototyping & Manufacturing: Fundamentals of Stereolithography, Society of Manufacturing Engineers, 1992.

[64] J.L. Hutter, J. Bechhoefer, Calibration of atomic-force microscope tips, Rev. Sci. Instrum. 64 (1993) 1868–1873.

[65] B.V. Derjaguin, V.M. Muller, Y.P. Toporov, Effect of contact deformations on the adhesion of particles, J. Colloid Interface Sci. 53 (1975) 314–326.

[66] H. Gojzewski, B. Imre, C. Check, R. Chartoff, G.J. Vancso, Mechanical mapping and morphology across the length scales unveil structure–property relationships in polycaprolactone based polyurethanes, J. Polym. Sci. B 54 (22) (2016) 2298–2310.

[67] P. Schön, K. Bagdi, K. Molnar, P. Markus, B. Pukanszky, G.J. Vancso, Quantitative mapping of elastic moduli at the nanoscale in phase separated polyurethanes by AFM, Eur. Polym. J. 47 (4) (2011) 692–698.

[68] H.J. Butt, B. Cappella, M. Kappl, Force measurements with the atomic force microscope: technique, interpretation and applications, Surf. Sci. Rep. 59 (1–6) (2005) 1–152.

[69] D.W. Collinson, R.J. Sheridan, M.J. Palmeri, L.C. Brinson, Best practices and recommendations for accurate nanomechanical characterization of heterogeneous polymer systems with atomic force microscopy, Prog. Polym. Sci. 119 (2021).

[70] H. Gojzewski, M. Sadej, E. Andrzejewska, M. Kokowska, Dataset for acrylate/silica nanoparticles formulations and photocured composites: viscosity, filler dispersion and bulk Poisson's ratio, Data Brief 12 (2017) 528–534.

[71] M. Tahmasebpoor, L. De Martín, M. Talebi, N. Mostoufi, J.R. Van Ommen, The role of the hydrogen bond in dense nanoparticle-gas suspensions, Phys. Chem. Chem. Phys. 15 (16) (2013) 5788–5793.

[72] J. Jakubiak, J.F. Rabek, Modeling of the kinetics of linear and crosslinking photopolymerization. Part III, Polimery/Polymers 46 (1) (2001) 10–22.

[73] M. Sadej-Bajerlain, H. Gojzewski, E. Andrzejewska, Monomer/modified nanosilica systems: photopolymerization kinetics and composite characterization, Polymer 52 (7) (2011) 1495–1503.

[74] F. Yeasmin, A.K. Mallik, A.H. Chisty, F.N. Robel, M. Shahruzzaman, P. Haque, et al., Remarkable enhancement of thermal stability of epoxy resin through the incorporation of mesoporous silica micro-filler, Heliyon 7 (1) (2021).

[75] W. Florkiewicz, D. Słota, A. Placek, K. Pluta, B. Tyliszczak, T.E.L. Douglas, et al., Synthesis and characterization of polymer-based coatings modified with bioactive ceramic and bovine serum albumin, J. Funct. Biomater. 12 (2) (2021).

[76] J.H. Lee, R.K. Prud'homme, I.A. Aksay, Cure depth in photopolymerization: experiments and theory, J. Mater. Res. 16 (12) (2001) 3536–3544.

[77] H. Yin, Y. Ding, Y. Zhai, W. Tan, X. Yin, Orthogonal programming of heterogeneous micro-mechano-environments and geometries in three-dimensional bio-stereolithography, Nat. Commun. 9 (1) (2018) 4096.

[78] A.K. O'Brien, C.N. Bowman, Modeling the effect of oxygen on photopolymerization kinetics, Macromol. Theory. Simul. 15 (2) (2006) 176–182.

[79] Chemours. Teflon FEP Information Bulletin (https://www.teflon.com/en/-/media/files/teflon/teflon-fep-film-tech-bulletin.pdf)..

[80] Y. Shan, A. Krishnakumar, Z. Qin, H. Mao, Reducing lateral stair-stepping defects in liquid crystal display-based vat photopolymerization by defocusing the image pattern, Addit. Manuf. 52 (2022).

[81] K. Engberg, C.W. Frank, Protein diffusion in photopolymerized poly(ethylene glycol) hydrogel networks, Biomed. Mater. 6 (5) (2011).

[82] P.F. Brune, G.S. Blackman, T. Diehl, J.S. Meth, D. Brill, Y. Tao, et al., Direct measurement of rubber interphase stiffness, Macromolecules 49 (13) (2016) 4909–4922.

[83] J. Song, R. Kahraman, D.W. Collinson, W. Xia, L.C. Brinson, S. Keten, Temperature effects on the nanoindentation characterization of stiffness gradients in confined polymers, Soft Matter 15 (3) (2019) 359–370.

[84] D.W. Collinson, M.D. Eaton, K.R. Shull, L.C. Brinson, Deconvolution of stress interaction effects from atomic force spectroscopy data across polymer-particle interfaces, Macromolecules 52 (22) (2019) 8940–8955.

[85] M. Sadej, H. Gojzewski, E. Andrzejewska, Photocurable polymethacrylate-silica nanocomposites: correlation between dispersion stability, curing kinetics, morphology and properties, J. Polym. Res. 23 (6) (2016) 116.

[86] H. Zou, S. Wu, J. Shen, Polymer/Silica Nanocomposites: preparation, characterization, propertles, and applications, Chem. Rev. 108 (9) (2008) 3893–3957.

[87] D.X. Hammer, A.J. Welch, G.D. Noojin, R.J. Thomas, D.J. Stolarski, B.A. Rockwell, Spectrally resolved white-light interferometry for measurement of ocular dispersion, J Opt Soc Am part A 16 (9) (1999) 2092–2102.

[88] M.L. Griffith, J.W. Halloran, Freeform fabrication of ceramics via stereolithography, J. Am. Ceram. Soc. 79 (10) (1996) 2601–2608.

[89] S. Westbeek, J.J.C. Remmers, J.A.W. van Dommelen, M.G.D. Geers, Multi-scale process simulation for additive manufacturing through particle filled vat photopolymerization, Comput. Mater. Sci. 180 (2020), 109647.